Influence of the electrode-electrolyte interface on electrochemical CO2 reduction reaction and hydrogen evolution reaction

Ye, C.

Citation

Ye, C. (2024, December 5). *Influence of the electrode-electrolyte interface on electrochemical CO2 reduction reaction and hydrogen evolution reaction*. Retrieved from https://hdl.handle.net/1887/4170871

A

Supplementary Information for Chapter 2

A.1 The morphology of working electrodes before electrochemical experiments

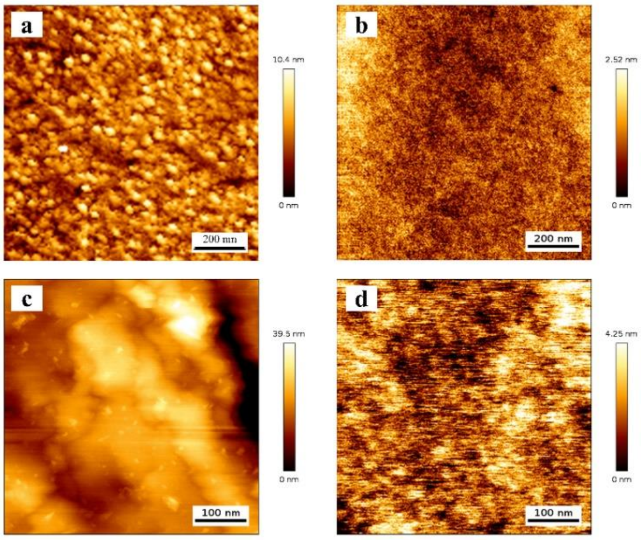

Figure A.1 AFM images of (a) poly Cu, (b) P4VP-modified Cu, (c) poly Au and (d) P4VP-modified Au in the air before all experiments.

A.2 Blank voltammetry and chronoamperometry experiments on unmodified and P4VP-modified pyrolytic graphite disk electrodes

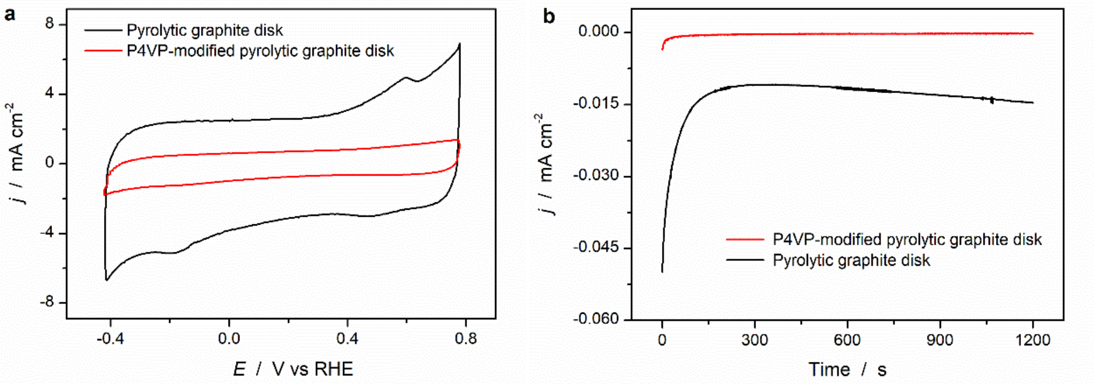

Figure A.2 (a) Cyclic voltammograms with scan rate 50 mV/s, and (b) total current density of CO_2 reduction on P4VP modified pyrolytic graphite (red curve) and unmodified pyrolytic graphite electrodes (black curve) at -0.6 V vs RHE in CO_2 saturated 0.1 M $KHCO_3$ solution. With reversible hydrogen electrode as reference electrode. All potentials were IR corrected.

A.3 Summary of vibrational bands assignments with different infrared spectroscopy

Table A.1 Vibrational Assignments of the ATR-SEIRAS bands

Surface	Band center / cm^{-1}	Species	Method	assignment
[1]	2343	solution CO_2	IR	ν_{COO}
Cu (110)[2-3]	2070	adsorbed CO on (100) or (111) step site	SNIFTIRS	
Cu (100)[4]	2050	adsorbed CO on (100) terrace	SNIFTIRS	
Cu single crystals,[5] poly Cu[6]	2001-1933	adsorbed CO on bridge site	SNIFTIRS	
[7]	1650	H_2O	IR	δ_{HOH}
poly Au[8] and poly Cu[9]	1620	solution HCO_3^-	ATR-SEIRAS	$\nu_{COO,\ asym}$
poly Cu[9]	1616-1608	adsorbed $HCOO^-$	ATR-SEIRAS	$\nu_{COO,\ asym}$
poly Cu,[9] Cu(100),[4] Au(111)[10]	1533-1508	adsorbed CO_3^{2-}	FTIR, IRAS	$\nu_{COO,\ asym}$
Poly Cu,[9] Au(111)[10] and poly Au[11]	1410	solution CO_3^{2-}	ATR	$\nu_{COO,\ asym}$
	1365	solution HCO_3^-	ATR	$\nu_{COO,\ sym}$
	1330	solution HCO_3^-	ATR-SEIRAS	

A.4 ATR-SEIRAS on poly Cu before adding P4VP layer

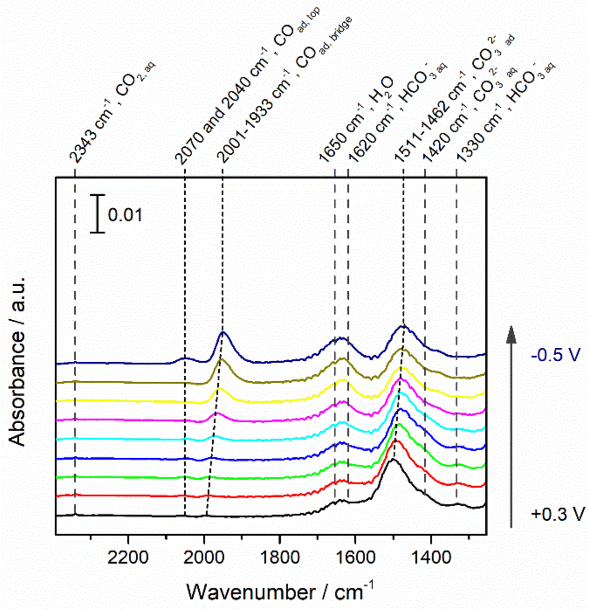

Figure A.3 ATR-SEIRA spectra of CO_2RR on poly Cu during linear sweep voltammetry at 1 mV/s from 0.3 V to -0.5 V vs RHE in CO_2 saturated 0.1M $KHCO_3$ aqueous solution. The background spectrum was taken at OCP in H_2O before experiments. The potential interval between spectra is 0.1 V.

A.5 ATR-SEIRAS on poly Au and P4VP-modified Au during CO_2RR

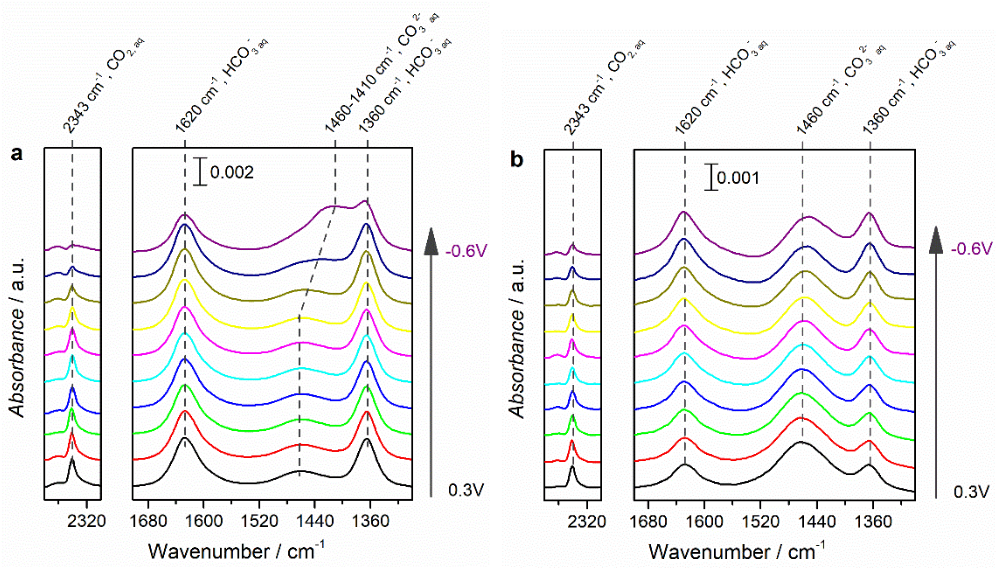

Figure A.4 ATR-SEIRA spectra of CO_2RR on the poly Au (a) and P4VP-modified Au (b) during linear sweep voltammetry at 1 mV/s from 0.3 V to -0.6 V vs RHE in CO_2 saturated 0.05M K_2CO_3 dissolved in D_2O. The background spectrum was taken at OCP in D_2O before experiments. The potential interval between spectra is 0.1 V.

The ratio of the integrals of the bands related to dissolved CO_2 and solution HCO_3^- (2343 and 1620 cm^{-1}, respectively; I_{CO2} / I_{HCO3^-}) was calculated as an indicator of local environment. To avoid the influence of H_2O bending band at 1650 cm^{-1}, D_2O was used to prepare the electrolyte. Bands related with dissolved CO_2, solution HCO_3^-, and solution CO_3^{2-} on unmodified and P4VP-modified Au electrodes are shown in Figures A.4 a and b respectively. Additionally, the bands related with solution HCO_3^- and solution CO_3^{2-} (at 1360 and 1460 cm^{-1}) show the same information of the different local environment changes on unmodified and P4VP-modified Au electrodes. When the potential went to -0.6 V vs RHE, the intensity of the band related with solution HCO_3^- decreases, while the intensity of the band related with solution CO_3^{2-} increases (compared with the bands intensity at 0.3 V vs RHE). Due to the growth of the broad band related with solution CO_3^{2-}, bands at 1360 and 1460 cm^{-1} overlap, which slightly shifts the band center of solution CO_3^{2-}. However, this observation does not have any effect on bands assignment nor on the calculated value of I_{CO2} / I_{HCO3^-}.

A.6 Contact angle measurements on the working electrodes before electrochemical experiments

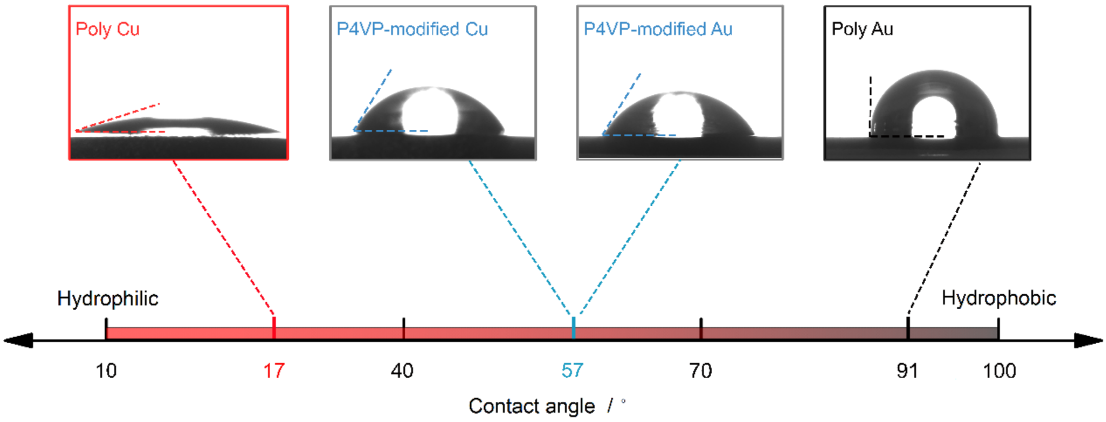

Figure A.5 Water contact angles on poly Cu, P4VP-modified Cu, poly Au and P4VP-modified Au surfaces.

A.7 Cyclic Voltammetry on P4VP-modified Cu and Au electrodes after CO_2RR

Cyclic Voltammetry was employed to characterize the electrodes after CO_2RR experiments. Although CO oxidation peak was observed on P4VP-modified Au electrode after CO_2RR at -0.5 V vs RHE,[12] the cyclic voltammograms on both P4VP-modified Cu and Au electrodes exhibit minor changes after applying negative potentials, as shown in the following cyclic voltammograms of P4VP-modified Cu and Au electrodes. This result indicates the intactness of the P4VP layer on poly Cu and Au surfaces after CO_2RR.

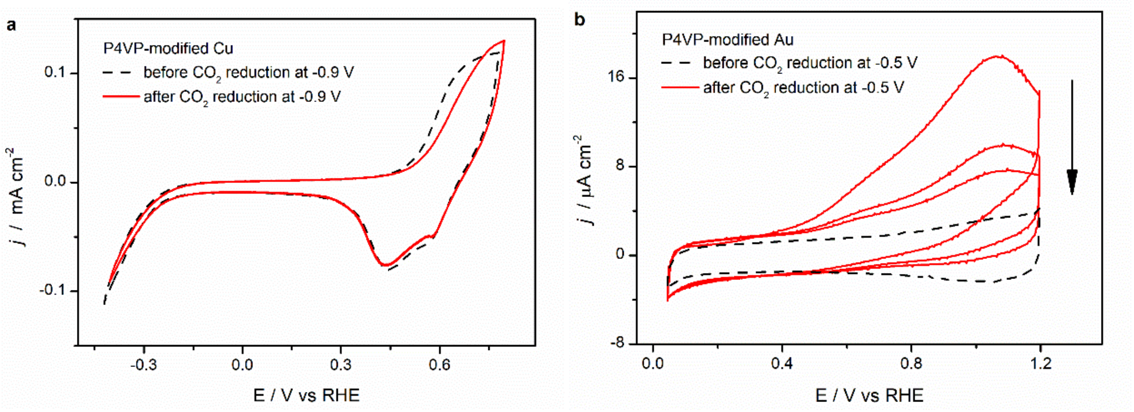

Figure A.6 Cyclic voltammograms of (a) P4VP-modified Cu after CO_2RR at -0.9 V vs RHE and (b) P4VP-modified Au after CO_2RR at -0.5 V vs RHE, measured at 50 mV/s in CO_2 saturated 0.1 M $KHCO_3$ solution.

References

1. Falk, M.; Miller, A. G., Infrared spectrum of carbon dioxide in aqueous solution. *Vib. Spectrosc* **1992,** *4*, 105-108.

2. Koga, O.; Teruya, S.; Matsuda, K.; Minami, M.; Hoshi, N.; Hori, Y., Infrared spectroscopic and voltammetric study of adsorbed CO on stepped surfaces of copper monocrystalline electrodes. *Electrochim. Acta* **2005,** *50* (12), 2475-2485.

3. Gunathunge, C. M.; Li, X.; Li, J.; Hicks, R. P.; Ovalle, V. J.; Waegele, M. M., Spectroscopic Observation of Reversible Surface Reconstruction of Copper Electrodes under CO_2 Reduction. *J. Phys. Chem. C* **2017,** *121* (22), 12337-12344.

4. Hori, Y.; Koga, O.; Watanabe, Y.; Matsuo, T., FTIR measurements of charge displacement adsorption of CO, on poly- and single crystal (100) of Cu electrodes. *Electrochim. Acta* **1998,** *44* (8-9), 1389-1395.

5. Shaw, S. K.; Berna, A.; Feliu, J. M.; Nichols, R. J.; Jacob, T.; Schiffrin, D. J., Role of axially coordinated surface sites for electrochemically controlled carbon monoxide adsorption on single crystal copper electrodes. *Phys. Chem. Chem. Phys.* **2011,** *13* (12), 5242-51.

6. Gunathunge, C. M.; Ovalle, V. J.; Li, Y.; Janik, M. J.; Waegele, M. M., Existence of an Electrochemically Inert CO Population on Cu Electrodes in Alkaline pH. *ACS Catal.* **2018,** *8* (8), 7507-7516.

7. Larsen, O. F.; Woutersen, S., Vibrational relaxation of the H_2O bending mode in liquid water. *J. Chem. Phys.* **2004,** *121* (24), 12143-5.

8. Ayemoba, O.; Cuesta, A., Spectroscopic Evidence of Size-Dependent Buffering of Interfacial pH by Cation Hydrolysis during CO_2 Electroreduction. *ACS Appl. Mater. Interfaces* **2017,** *9* (33), 27377-27382.

9. Moradzaman, M.; Mul, G., Infrared Analysis of Interfacial Phenomena during Electrochemical Reduction of CO_2 over Polycrystalline Copper Electrodes. *ACS Catal.* **2020,** *10* (15), 8049-8057.

10. Arihara, K.; Kitamura, F.; Ohsaka, T.; Tokuda, K., Characterization of the adsorption state of carbonate ions at the Au(111) electrode surface using in situ IRAS. *J. Electroanal. Chem.* **2001,** *510*, 128-135.

11. Dunwell, M.; Yang, X.; Setzler, B. P.; Anibal, J.; Yan, Y.; Xu, B., Examination of Near-Electrode Concentration Gradients and Kinetic Impacts on the Electrochemical Reduction of CO_2 using Surface-Enhanced Infrared Spectroscopy. *ACS Catal.* **2018,** *8* (5), 3999-4008.

12. Marcandalli, G.; Villalba, M.; Koper, M. T. M., The Importance of Acid-Base Equilibria in Bicarbonate Electrolytes for CO_2 Electrochemical Reduction and CO Reoxidation Studied on Au(hkl) Electrodes. *Langmuir* **2021,** *37* (18), 5707-5716.

B

Supplementary Information for Chapter 3

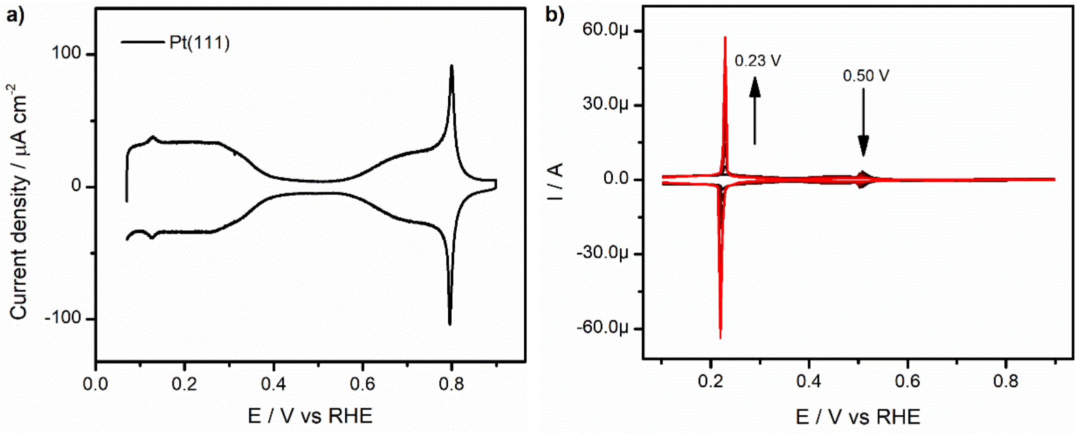

Figure B.1 (a). Cyclic voltammogram of Pt(111) in 0.1 M $HClO_4$. Scan rate: 50 mV s^{-1}. (b). Cyclic voltammograms for Pt(111) in 0.1 M H_2SO_4 + 0.1 mM $PdSO_4$, recorded in successive stages during Pd deposition experiment. Scan rate: 50 mV s^{-1}. Arrows indicate the evolution with time.

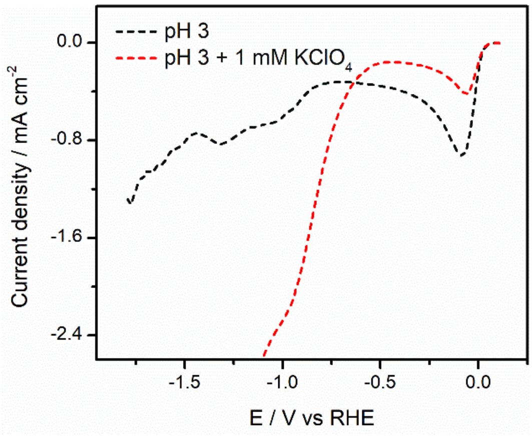

Figure B.2 Linear Sweep Voltammetry of $Pd_{ML}Pt(111)$ in argon-purged pH 3 electrolytes in the absence (black) and presence of 1 mM $KClO_4$ (red). Scan rate: 10 mV/s.

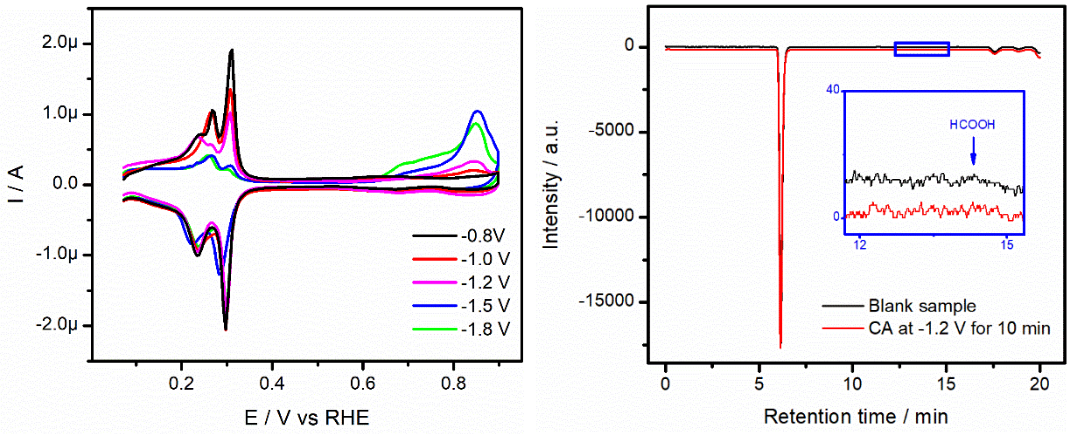

Figure B.3 (a). CO stripping voltammograms on $Pd_{ML}Pt(111)$ after CO_2 reduction at different vertex potentials in CO_2-saturated pH 3 electrolyte without metal cations, measured at 10 mV s^{-1}. (b). HPLC data before and after chronoamperometry at -1.2 V_{RHE} for 10 min in CO_2-saturated pH 3 electrolyte without metal cations.

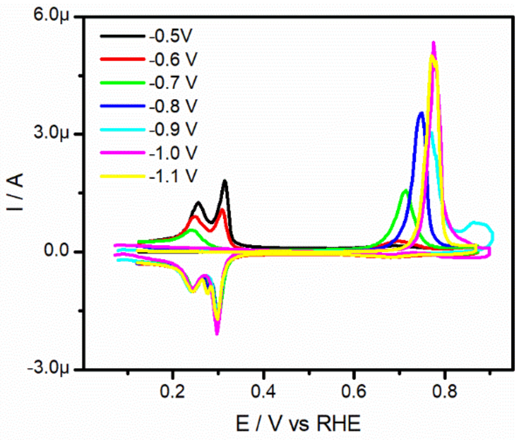

Figure B.4 CO stripping voltammograms on $Pd_{ML}Pt(111)$ after CO_2 reduction at different vertex potentials in CO_2-saturated pH 3 with 1 mM $KClO_4$ electrolyte, measured at 10 mV s^{-1}.

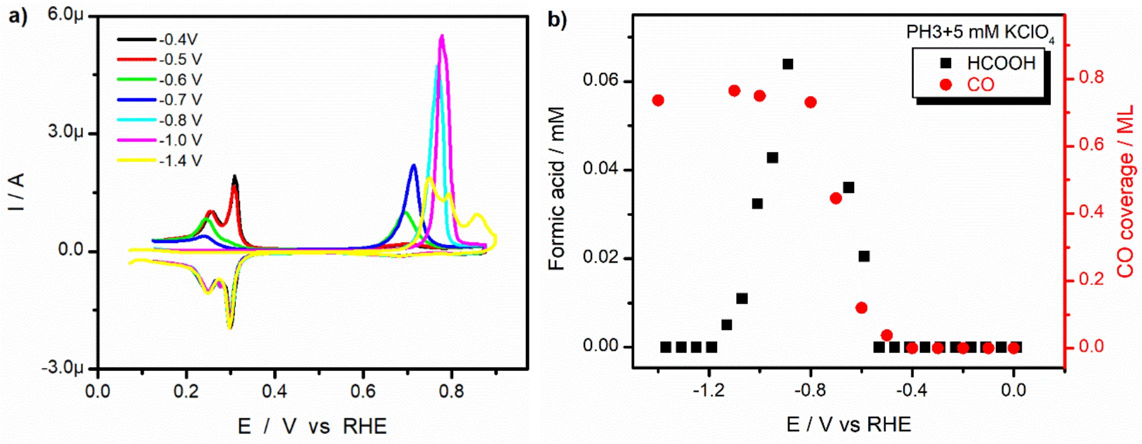

Figure B.5 (a). CO stripping voltammograms on $Pd_{ML}Pt(111)$ after CO_2 reduction at different vertex potentials in CO_2-saturated pH 3 with 5 mM $KClO_4$ electrolyte, measured at 10 mV s^{-1}. (b). HCOOH formation and the calculated CO coverage as a function of potential.

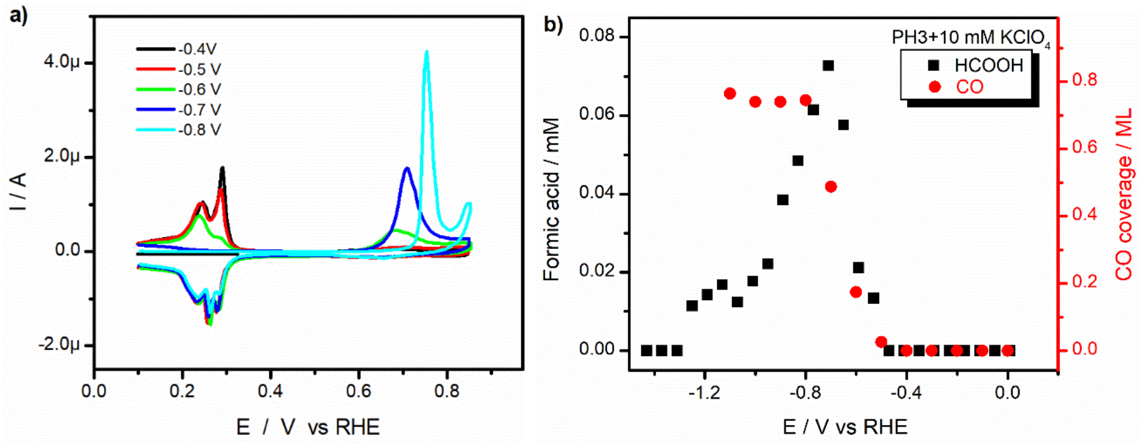

Figure B.6 (a). CO stripping voltammograms on $Pd_{ML}Pt(111)$ after CO_2 reduction at different vertex potentials in CO_2-saturated pH 3 with 10 mM $KClO_4$ electrolyte, measured at 10 mV s^{-1}. (b). HCOOH formation and the calculated CO coverage as a function of potential.

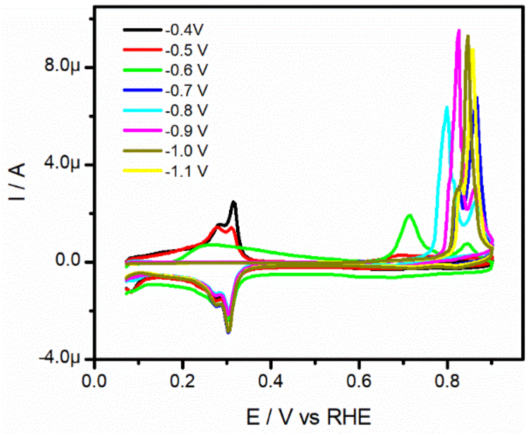

Figure B.7 CO stripping voltammograms on $Pd_{ML}Pt(111)$ after CO_2 reduction at different vertex potentials in CO_2-saturated pH 3 with 99 mM $KClO_4$ electrolyte, measured at 10 mV s^{-1}.

Figures B.3a, B.4, B.5a, B.6a and B.7 show oxidative stripping voltammograms of adsorbed CO obtained during CO_2RR by increasing the vertex potential in steps of 0.1 V from -0.4 V_{RHE}. With the positive going scan, decreasing peaks (peak at 0.31 V_{RHE} decreasing first) in the potential region between +0.05 and +0.35 V_{RHE} suggest adsorbed CO. CO_{ads} oxidation peaks are observed in the potential region between +0.65 and +0.9 V_{RHE}, the peaks varying under different conditions. These different CO oxidation peaks may result from different *CO coverage or changes of local electrolyte after CO_2RR. After oxidation of *CO, the typical CV features in pH 3 electrolyte are again observed in the negative going scan. In some voltammograms, CV features of $Pd_{ML}Pt(111)$ slightly deviate from the standard, which might be due to minor loss of Pd atoms during CO_2RR. Moreover, peaks in the potential region between +0.05 and +0.35 V_{RHE} decreases with increasing of *CO obtained from CO_2RR, which leads to more CO oxidation current in potential region between +0.65 and +0.9 V_{RHE} and corresponding higher CO coverage.

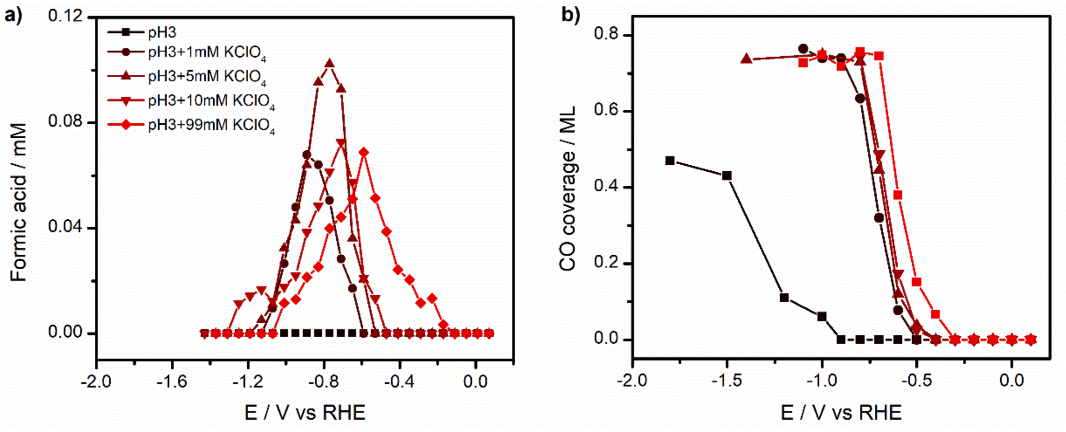

Figure B.8 A summary of (a) formic acid and (b) CO generation during CO_2RR in CO_2 saturated pH 3 electrolytes in the presence of 0, 1, 5, 10, 99 mM $KClO_4$.

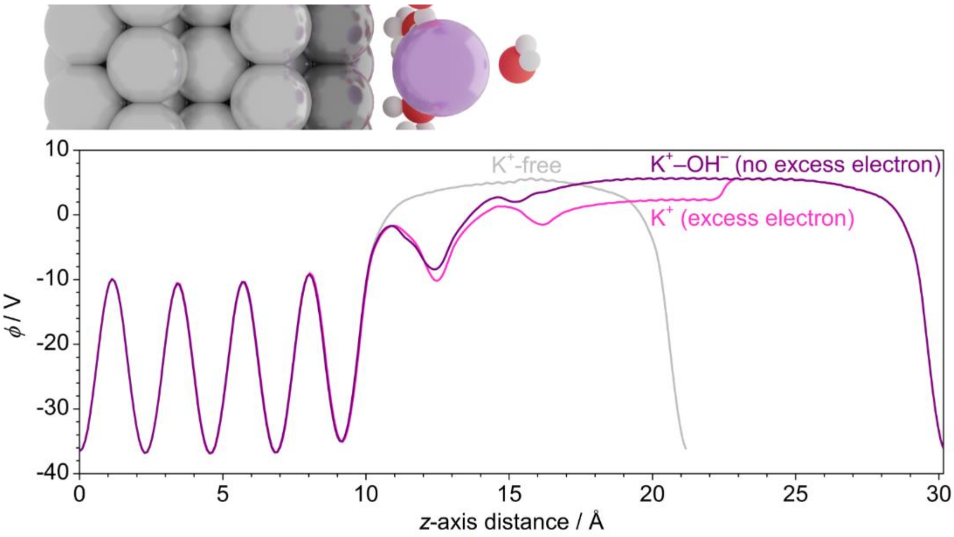

Figure B.9 Electrostatic potential (Φ) profile across the simulation cell (z-direction, reported on top) for the cation-free (gray line) and near-cation ($d_{K+\text{-surf}}$ = 4 Å) systems with and without excess electron (magenta and purple line respectively).

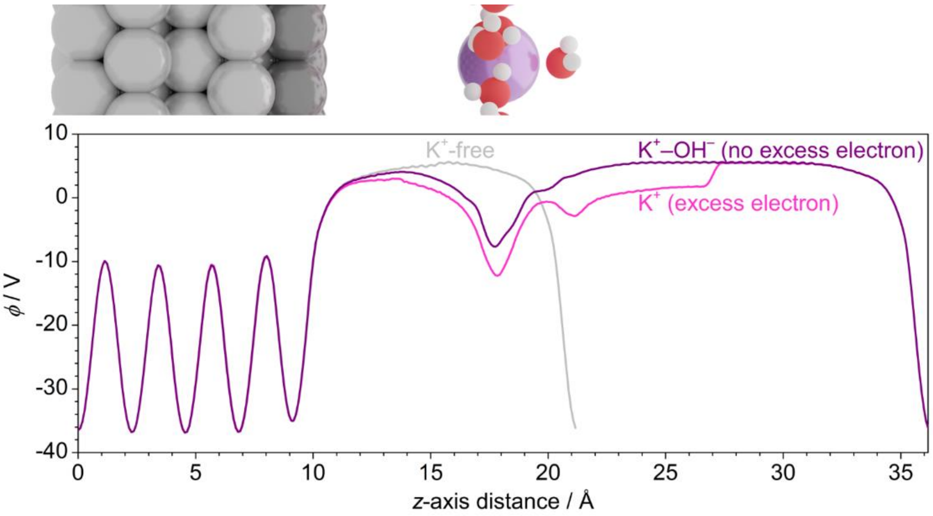

Figure B.10 Electrostatic potential (Φ) profile across the simulation cell (*z*-direction, reported on top) for the cation-free (gray line) and far-cation ($d_{K+\text{-surf}}$ = 9 Å) systems with and without excess electron (magenta and purple line respectively).

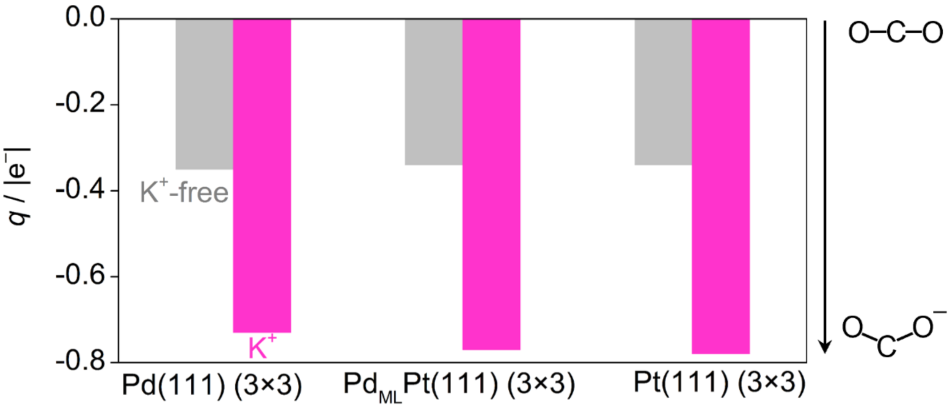

Figure B.11 Bader charges for adsorbed CO_2^- on Pd(111) (3×3), Pd$_{ML}$Pt(111) (3×3), and Pt(111) (3×3). The gray column reports the baseline case for the adsorbate without K^+, while the near-K^+ system (with excess electron) is indicated in magenta. Solvated K^+ was here simulated with three water molecules within its coordination shell.

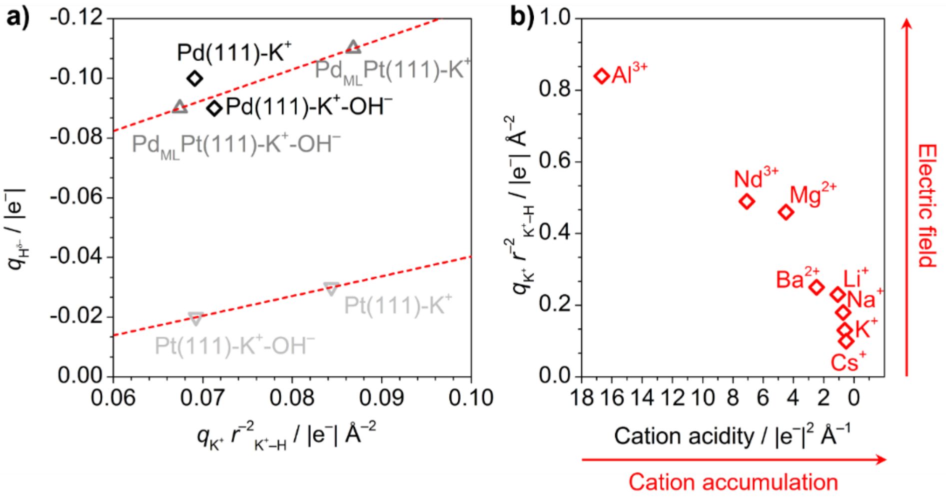

Figure B.12 (a). Correlation between $H^{\delta-}$ Bader charges and cation-induced electric field, proportional to $q^{K+}/r^2_{K+\text{-}H}$. (b). Cation-induced electric field vs cation acidity for alkali, bi-valent, and tri-valent cations. Cation acidity affects cation accumulation, while electric field favors the formation of hydrides on the surface. The distance between cation and hydrogen is here taken as the state-of-the-art cation-water distance reported for solvated cations (see Table B.3).[5-6]

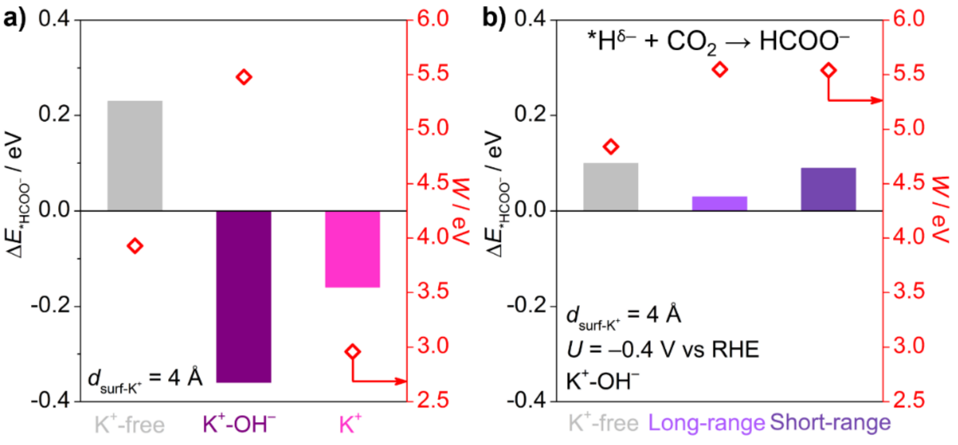

Figure B.13 (a). DFT energy on $Pd_{ML}Pt(111)$ (3×3) relative to cation-induced outer-sphere CO_2 activation to $HCOO^-$ for the K^+-free (gray) and near-K^+ with and without balancing OH^- (purple and magenta) for different values of metal work functions (right *y*-axis). (b). DFT energy relative to the $HCOO^-$ formation step on $Pd_{ML}Pt(111)$ (3×3) supercell for cation-free (gray), far-K^+ (light purple), and near-K^+ (dark purple) cases at U = -0.4 V vs RHE. Values of metal work function for clean surfaces are given at the right *y*-axis. For details on the model, see Figure 3.5a-b and Computational Details.

Table B.1 Calculated work function for the $Pd_{ML}Pt(111)$ (3×3) surface for clean surface and $*CO_2$ for the K^+-free, the near-K^+ ($d_{K+\text{-surf}}$ = 4 Å), and far-K^+ ($d_{K+\text{-surf}}$ = 9 Å) cases, with and without balancing OH^-. Cation and H_2O molecules (within bracket) were absent in the K^+-free case.

System	W / eV				
	K^+-free	Near K^+	Near K^+ + OH^-	Far K^+	Near K^+ + OH^-
Clean surface	+4.84	+2.35	+5.54	+1.74	+5.55
$*CO_2^-$ (+ K^+ + $5H_2O$)	+5.05	+5.09	+5.59	+5.14	+5.41

Table B.2 Calculated Bader charges of the $Pd_{ML}Pt(111)$ (3×3) surface for clean surface and $*CO_2$ for the K^+-free, the near-K^+ ($d_{K+\text{-surf}}$ = 4 Å), and far-K^+ ($d_{K+\text{-surf}}$ = 9 Å) cases, with and without balancing OH^-. Cation and H_2O molecules (within brackets) were absent in the K^+-free case.

System	q_{surf} / $|e^-|$				
	K^+-free	Near-K^+	Near K^+ + OH^-	Far K^+	Near K^+ + OH^-
Clean surface	+0.00	–0.62	–0.24	–0.05	–0.05
$*CO_2^-$ (+ K^+ + $5H_2O$)	+0.35	–0.07	+0.29	+0.30	+0.30

Table B.3 Properties of alkali, bi-valent, and tri-valent cations, taken from Refs. [5-8].

Cation	q_{cat} / $|e^-|$	ionic radius / Å	$d_{cat\text{-}O}$ / Å	Acidity / $|e^-|^2$ $Å^{-1}$	$q_{cat}/r^2_{cat\text{-}O}$ / $|e^-|$ $Å^{-2}$
Li^+	1	0.92	2.08	1.09	0.23
Na^+	1	1.39	2.36	0.72	0.18
K^+	1	1.64	2.80	0.61	0.13
Cs^+	1	1.88	3.14	0.53	0.10
Mg^{2+}	2	0.89	2.09	4.49	0.46
Ba^{2+}	2	1.61	2.81	2.48	0.25
Al^{3+}	3	0.54	1.89	16.67	0.84
Nd^{3+}	3	1.27	2.47	7.09	0.49

References

1. McCrum, I. T.; Koper, M. T. M., The role of adsorbed hydroxide in hydrogen evolution reaction kinetics on modified platinum. *Nature Energy* **2020,** *5* (11), 891-899.
2. Monteiro, M. C.; Dattila, F.; Hagedoorn, B.; García-Muelas, R.; López, N.; Koper, M., Absence of CO_2 electroreduction on copper, gold and silver electrodes without metal cations in solution. *Nat. Catal.* **2021,** *4* (8), 654-662.
3. Chan, K.; Nørskov, J. K., Potential Dependence of Electrochemical Barriers from ab Initio Calculations. *J. Phys. Chem. Lett.* **2016,** *7* (9), 1686-1690.
4. Chan, K.; Nørskov, J. K., Electrochemical Barriers Made Simple. *J. Phys. Chem. Lett.* **2015,** *6* (14), 2663-2668.
5. Monteiro, M. C. O.; Dattila, F.; Lopez, N.; Koper, M. T. M., The Role of Cation Acidity on the Competition between Hydrogen Evolution and CO2 Reduction on Gold Electrodes. *J. Am. Chem. Soc.* **2022,** *144* (4), 1589-1602.
6. Marcus, Y., Ionic radii in aqueous solutions. *Chem. Rev.* **1988,** *88* (8), 1475-1498.
7. Haynes, W. M., *CRC handbook of chemistry and physics*. CRC press: 2016.
8. Waegele, M. M.; Gunathunge, C. M.; Li, J.; Li, X., How cations affect the electric double layer and the rates and selectivity of electrocatalytic processes. *J. Chem. Phys.* **2019,** *151* (16), 160902.

C

Supplementary Information for Chapter 4

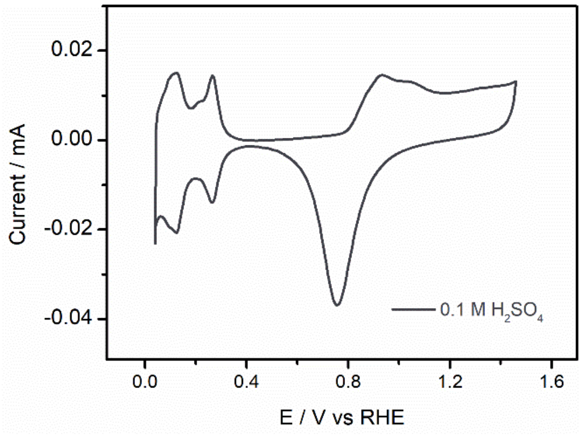

Figure C.1 Cyclic voltammetry of the polycrystalline Pt rotation disk electrode after electrochemical polishing in 0.1 M H_2SO_4, scan rate: 50 mV s^{-1}.

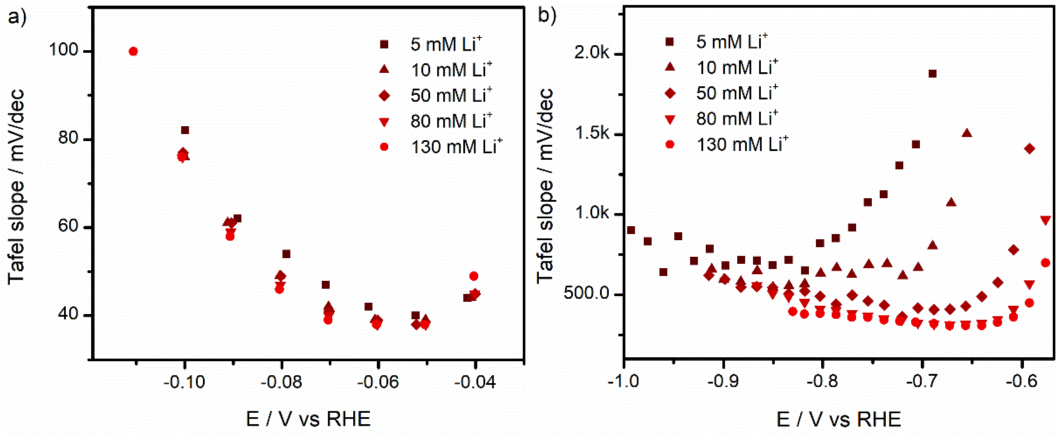

Figure C.2 Tafel slope plots for a) proton reduction and b) water reduction reaction derived from the linear sweep voltammograms of Figure 4.1a.

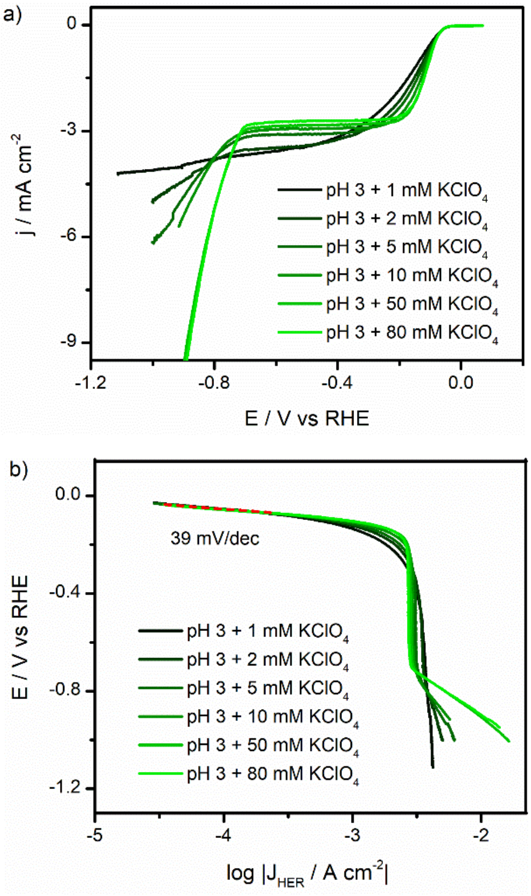

Figure C.3 (a) Linear sweep voltammograms obtained for HER on Pt polycrystalline surface at 2400 rpm in pH 3 electrolytes with the presence of 1, 2, 5, 10, 50 and 80 mM $KClO_4$. The voltammograms were recorded at 10 mV s^{-1}. (b) Tafel slope analysis derived from the linear sweep voltammograms in (a), the range used for fitting is indicated in all plots with a dotted line in red.

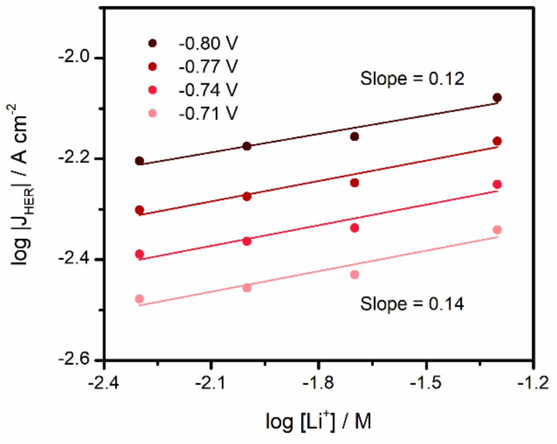

Figure C.4 A cation concentration reaction order plot for HER on a polycrystalline Pt electrode at 2400 rpm in pH 3 + 80 mM $KClO_4$ + x mM LiClO4, at 30 mV potential steps (vs RHE) plotted as a function of the logarithm of the current density on the y-axis and logarithm of Li^+ concentration on the x-axis. The corresponding slopes (reaction orders) at applied potentials of -0.80 V and -0.71 V (vs RHE) are respectively indicated next to the plots.

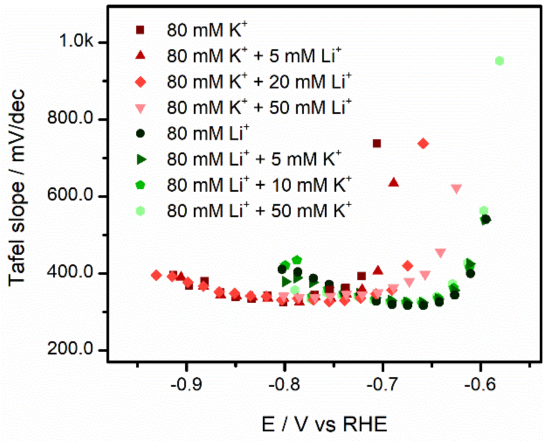

Figure C.5 Tafel slopes for water reduction reaction on polycrystalline Pt in pH 3 electrolytes at a rotation rate of 2400 rpm at a scan rate of 10 mV s^{-1}.

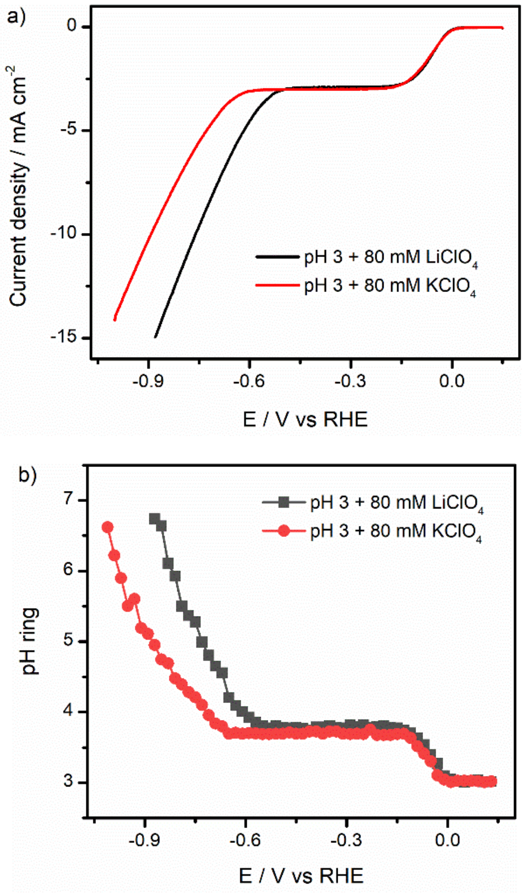

Figure C.6 (a) Linear sweep voltammograms of the Pt disk electrode at 2400 rpm and 10 mV s^{-1} in pH 3 electrolytes in the presence of 80 mM $LiClO_4$ and $KClO_4$ respectively. (b) The interfacial pH at the Au ring electrode during the linear sweep voltammetry on the Pt disk electrode.

D

Supplementary Information for Chapter 5

Energy efficiency calculation:

$$\varepsilon_{energy} = \frac{(E^{0}_{CO2}+E^{0}_{O2})*FE_{CO2RR\ product}}{E_{cell}} \qquad \text{Supplementary Equation 1}$$

Where E^0 are the standard potentials of the cathode to desired products and anode reactions, FE is the current efficiency as percentage, and E_{cell} is the cell potential in V.

Table D.1 Bulk pH of the electrolytes before the electrolysis (after CO_2 saturation), after 5h electrolysis (1 h electrolysis at a total current density of 10 mA cm^{-2}, 1 h electrolysis at a total current density of 50 mA cm^{-2}, 1 h electrolysis at a total current density of 75 mA cm^{-2}, 1 h electrolysis at a total current density of 100 mA cm^{-2} and 1 h electrolysis at a total current density of 150 mA cm^{-2}), and after 20h electrolysis at a total applied current density of 200 mA cm^{-2}.

Solutions	pH before electrolysis (after CO_2 saturation)	pH after 5h electrolysis	pH after 20h electrolysis
0.5 M $KHCO_3$	7.23[1]	7.47	7.8
pH 3+0.25 M K_2SO_4	3.01	2.96	2.46

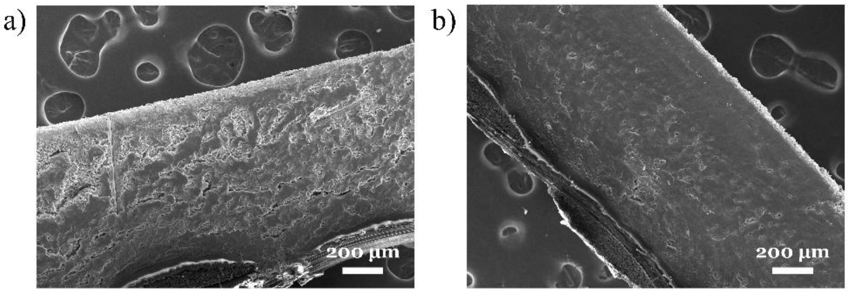

Figure D.1 SEM images of cross sections of Copper GDE after 20 hours long term electrolysis at a total applied current density of 200 mA cm^{-2} in pH 3 electrolyte with presence of 0.25M K_2SO_4.

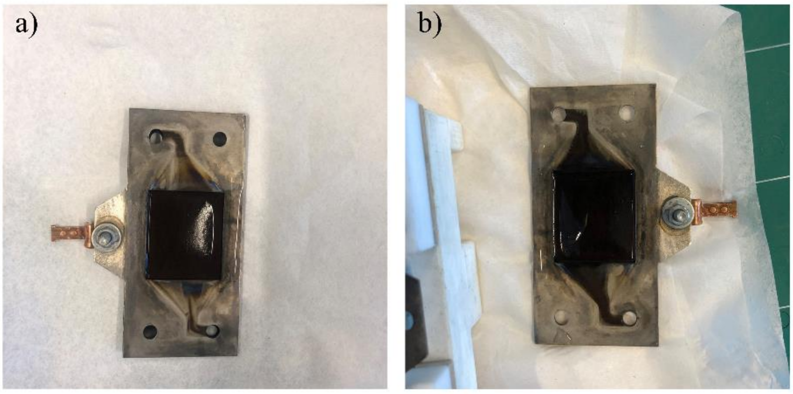

Figure D.2 Images of copper GDEs after 20 hours long term electrolysis at a total applied current density of 200 mA cm^{-2} in a) 0.5M $KHCO_3$ and b) pH 3 electrolyte with presence of 0.25M K_2SO_4 respectively.

Reference

1. Chen, C.; Zhang, B.; Zhong, J.; Cheng, Z., Selective electrochemical CO_2 reduction over highly porous gold films. *Journal of Materials Chemistry A* **2017,** *5* (41), 21955-21964.